Geophysical Journal International

Geophys. J. Int. (2015) **201,** 1335–1345 doi: 10.1093/gji/ggv063
GJI Seismology

Recorded displacements in a landslide slope due to regional and teleseismic earthquakes

L. Lenti,[1] S. Martino,[2] A. Paciello,[3] A. Prestininzi[2] and S. Rivellino[2]

[1] *Institut Français des Sciences et Technologies des Transports, de l'Aménagement et des Réseaux (IFSTTAR-Paris)* – 14-20 *Boulevard Newton Cité Descartes, Champs sur Marne, F-*77447 *Marne la Vallée Cedex* 2*, France*
[2] *Dipartimento di Scienze della Terra and Research Center for Geological Risks CERI, Università di Roma "Sapienza", P.le A. Moro* 5*, I-*00185 *Roma, Italy. E-mail: salvatore.martino@uniroma1.it*
[3] *Agenzia Nazionale per le Nuove Tecnologie, l'Energia e lo Sviluppo Economico Sostenibile (ENEA Casaccia) - Via Anguillarese* 301*, I-*00060 *S. Maria di Galeria, Roma, Italy*

Accepted 2015 February 9. Received 2015 February 6; in original form 2014 June 20

SUMMARY

Regional and teleseismic earthquakes can induce displacements along joints in a landslide-involved rocky slope in Central Italy. The rarity of these effects is due to specific physical properties of the seismic signals associated with: (i) the energy content, (ii) the distribution of relative energy and peak of ground acceleration related to the ground motion components and (iii) the spectral amplitude distribution in the frequency domain; these properties allow the triggering earthquakes to be distinguished from the others. The observed effects are relevant when compared to the direction of the landslide movement and the dimensions of the involved rock mass volume. The landslide movement is less constrained in the direction parallel to the dip of the slope and the landslide dimensions are associated with characteristic periods that control the landslide deformational response in relation to the spectral content of the ground motion. The earthquake-induced displacements are significant because they have the same order of magnitude as the average annual cumulative displacement based on a decade of strain measurements within the slope.

Key words: Geomorphology; Geomechanics; Site effects.

1 INTRODUCTION

The effects of near-field earthquakes on slopes have been largely discussed and constrained by experimental data (Rodríguez *et al.* 1999; Sepulveda *et al.* 2005a,b; Alfaro *et al.* 2012; Jousset *et al.* 2013). This study instead focuses on the interaction between regional earthquakes (RGE) or teleseismic earthquakes (TSE) and unstable slopes, with particular reference to the experimental evidence of earthquake-induced displacements along monitored rock mass joints. The RGE and the TSE are here distinguished as the former ones are mainly characterized by crustal attenuation of the seismic waves, i.e. focal distances of hundreds of kilometres, (Van der Elst & Brodsky 2010 and citations therein) while the latter ones are related to earthquakes focused at very far distances, in the order of thousands of kilometres, and result in records of waveforms with long to very long periods (Pomeroy *et al.* 1982).

Since the 1970s, the interactions of inertial forces due to long or very long period dynamic accelerations (induced, for instance, by tides or TSE) on entire slopes have been demonstrated worldwide. Several examples have involved volcanic activity, volcano-tectonic flank deformations (Johnston & Mauk 1972; McNutt & Beavan 1981; Rydelek *et al.* 1988; Kasahara 2002; Myiazawa *et al.* 2005; Sottili *et al.* 2007), and, more recently, interplate slow-slip events (Hollingsworth *et al.* 2007; Itaba & Ando 2011). RGE and TSE are also cited to explain documented large landslide re-activations (Bozzano *et al.* 2011; Delgado *et al.* 2011; Jousset & Rohmer 2012) and to attribute mechanical properties to landslide masses (Brodsky *et al.* 2003).

The here presented study is based on data recorded by an integrated monitoring system that allows to record both displacements along joints and seismic events. This system has been in operation since September 2008 in the Peschiera Spring slope, which is located in the San Vittorino plain (Central Apennines, Italy; Fig. 1) and hosts the major drainage plant of Rome aqueduct. The monitoring system was installed within the tunnels to manage the geological risk of the plant; at this aim, the collected data were analysed for security plans in case of a seismic crisis (Lenti *et al.* 2012). The Peschiera Spring slope is characterized by a highly jointed carbonate rock mass of Mesozoic and Tertiary limestones and marly limestones and is involved in a landslide. A high-resolution (2 m) digital elevation model (DEM) of the slope derived from a LIght Detection And Ranging (LIDAR) remote survey enabled the identification of numerous gravity-induced morphological elements (e.g. scarps, trenches, sinkholes and tension cracks; Figs 2 and 3;

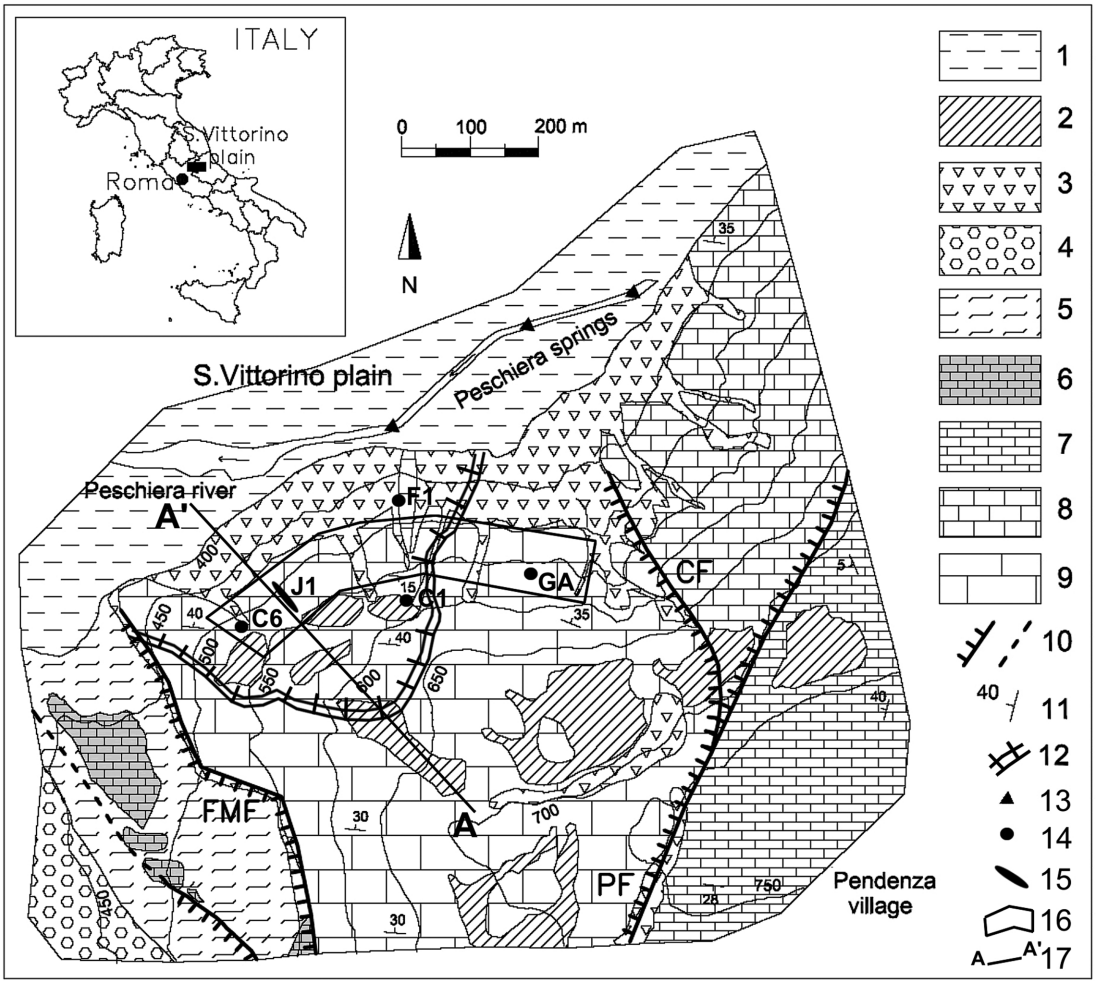

Figure 1. Location and geological sketch of the monitored slope: (1) Recent alluvia; (2) Reddish soils; (3) Slope debris; (4) Gravel and conglomerate (upper-Pliocene and lower-Pleistocene portions); (5) Sandy-clayey flysch (upper Miocene); (6) Marly limestone (upper Cretaceous–lower Miocene); (7) Birdseye micritic limestone (lower Cretaceous); (8) Coral limestone (upper Malm); (9) Coral and echinoid limestone (Malm portion); (10) Fault (dashed if estimated): FMF, Fiamignano-Micciani Fault; CF, Canalone Fault; PF, Pendenza Fault; (11) Strike and dip of strata; (12) Perimeter trench of the landslide volume; (13) Peschiera Springs; (14) Accelerometric stations (C1, GA, F1 and C6) installed within the drainage plant; (15) Monitored joint J1 within the drainage plant; (16) Sector of the slope with strain-gauge and extensometer installations within the drainage tunnels; (17) trace of cross-section A–A′ of Fig. 2.

Lenti *et al.* 2012). These landforms confirm that slow, intense and pervasive deformation affects the entire slope (Martino *et al.* 2004; Maffei *et al.* 2005) due to a complex deep-seated gravitational slope deformation (DSGSD *Auct.*), consisting in a mass rock creep (MRC; Zischinsky 1969; Savage & Varnes 1987; Chigira 1992) that continuously evolves from rock mass spreading (Hutchinson 1988) to rock block mass deformation (Martino *et al.* 2004). In particular, based on a frontal 3-D view of the slope (Fig. 3), the rock mass spreading can be observed clearly in the western portion of the slope, where it is associated with a radial displacement field and generates continuous transverse scarps combined with longitudinal trenches (i.e. multiple transverse trenches). In the eastern sector of the slope, a previous rock mass failure can be observed in the DEM. This failure generated two debris fans clearly visible at the bottom of the slope. The lateral 3-D view of the slope shows that the spreading process attributes a convex shape to the involved sector of the slope while the already collapsed one reveals a concave shape (Fig. 3).

Geomechanical surveys consisting in joint measurements on rock mass outcrops, indicate that the main recognized joint sets are consistent with the observed morphological and structural elements (Martino *et al.* 2004). Particularly significant is the correlation among (i) the roughly E-W-trending joint set and tension cracks detected along the slope, (ii) the N45°W ± 5° and N45°E ± 10° joint sets, transversal scarps and main tectonic elements (i.e. the faults reported in Fig. 1) and (iii) the approximately N–S-trending subvertical joint set and trench scarps. Finally, secondary joint sets (N45°W ± 5° and N30°E ± 5° that dip S at 40–50°) may be regarded as complementary to those previously mentioned. The main geomechanical joint parameters derived from field and laboratory tests (Maffei *et al.* 2005) are summarized in Table 1. In particular, the monitored joint J1 of Fig. 1, ascribable to the N45°W set, can be regarded as a suitable detector of the landslide movement, because it bounds a main sliding block (Fig. 2).

The seismic events recorded so far within the Peschiera Spring slope were analysed in relation to the data obtained by the stress–strain monitoring system to infer possible relationships among the detected deformations, ongoing gravitational processes and observed earthquakes (Lenti *et al.* 2012).

Such a monitoring integrated system provided, for the first time, records of displacements along joint J1 induced by RGE and TSE. The here collected evidences allowed to discuss the role of certain

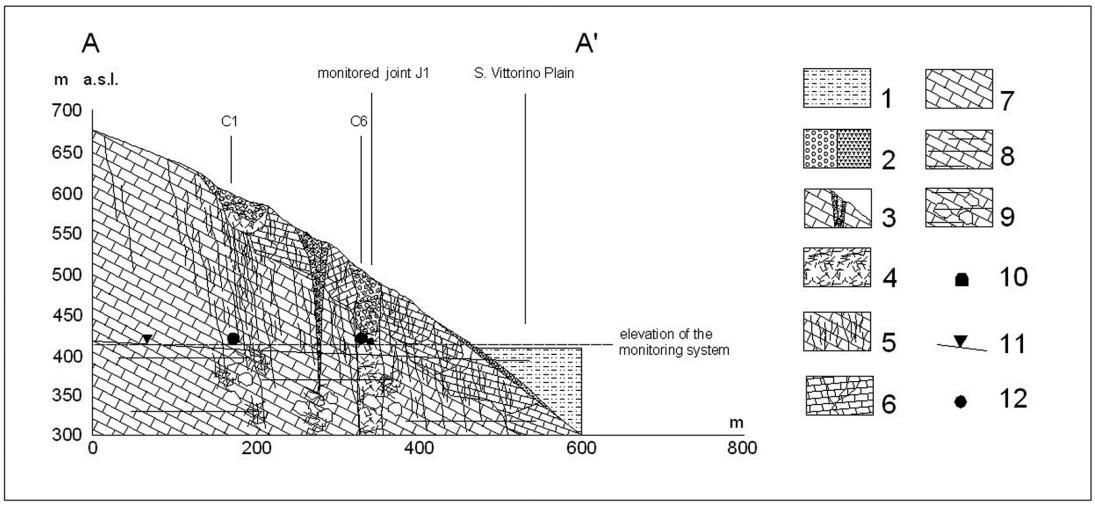

Figure 2. Geological cross section along trace A–A′ of Fig. 1: (1) Alluvial deposit of the S. Vittorino plain; (2) Trench and slope debris (left and right, respectively); (3) Sinkhole; (4) Intensely jointed rock mass; (5) Concentration of cracks in the rock mass; (6) Dislodged rock mass; (7) Rock mass located above the water table; (8) Rock mass located in the karst aquifer; (9) Underground caves in the karst aquifer; (10) Drainage plant tunnel; (11) Level of groundwater and (12) Projection of the accelerometric station shown in Fig. 1 by considering a 200 m width buffer.

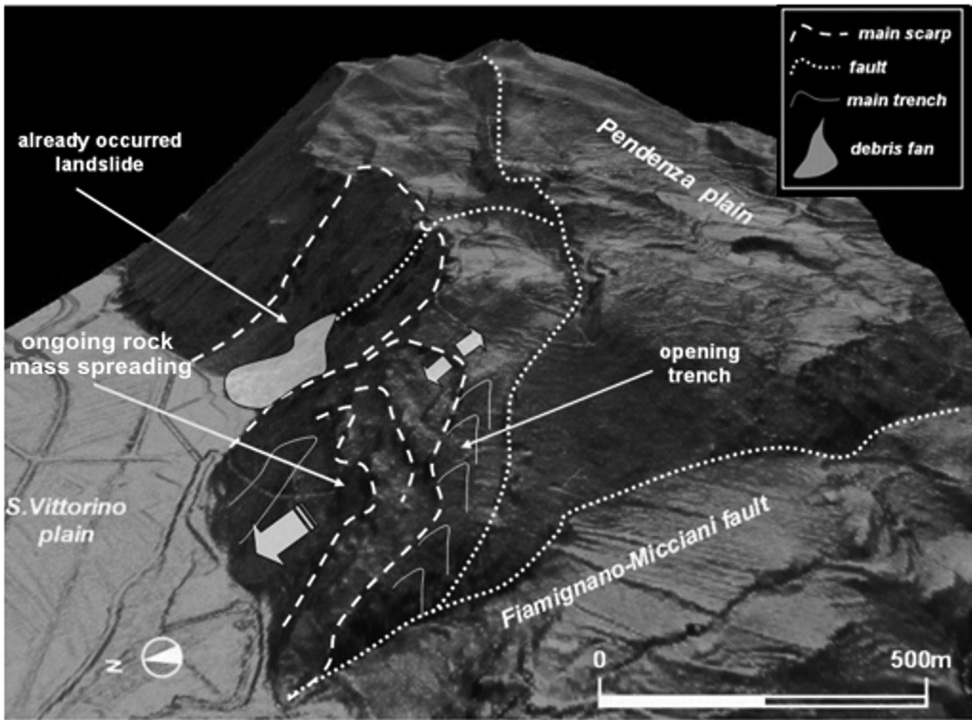

Figure 3. 3-D views of the Peschiera Springs slope obtained from the 2-m-resolution DEM illustrating the rock mass volume involved in the ongoing landslide processes and showing the main generated landforms. The profile of the slope illustrates the convex shape of the western sector, presently involved in the spreading process, and the concave shape of the already collapsed eastern sector. The northward direction of the rock mass movement is indicated by arrows; the boundaries of the landslide volume are depicted by dashed white lines.

Table 1. Geomechanical parameters of rock mass and joints outcropping on the slope as derived by in situ and laboratory measurements: den, density; G, shear modulus; *c*, cohesion (in case of joints it is due to the fill materials or to the concrete); Φ, friction angle and *t*, tensile strength; na, not available.

	Den (kg m^{-3})	*G* (N m s^{-2})	*c* (N m s^{-2})	Φ (°)	*t* (N m s^{-2})
Calcareous rock mass	2690	2.35E+09	3.00E+07	46	1.50E+07
Joint	na	na	2.00E+05	35	1.68E+05

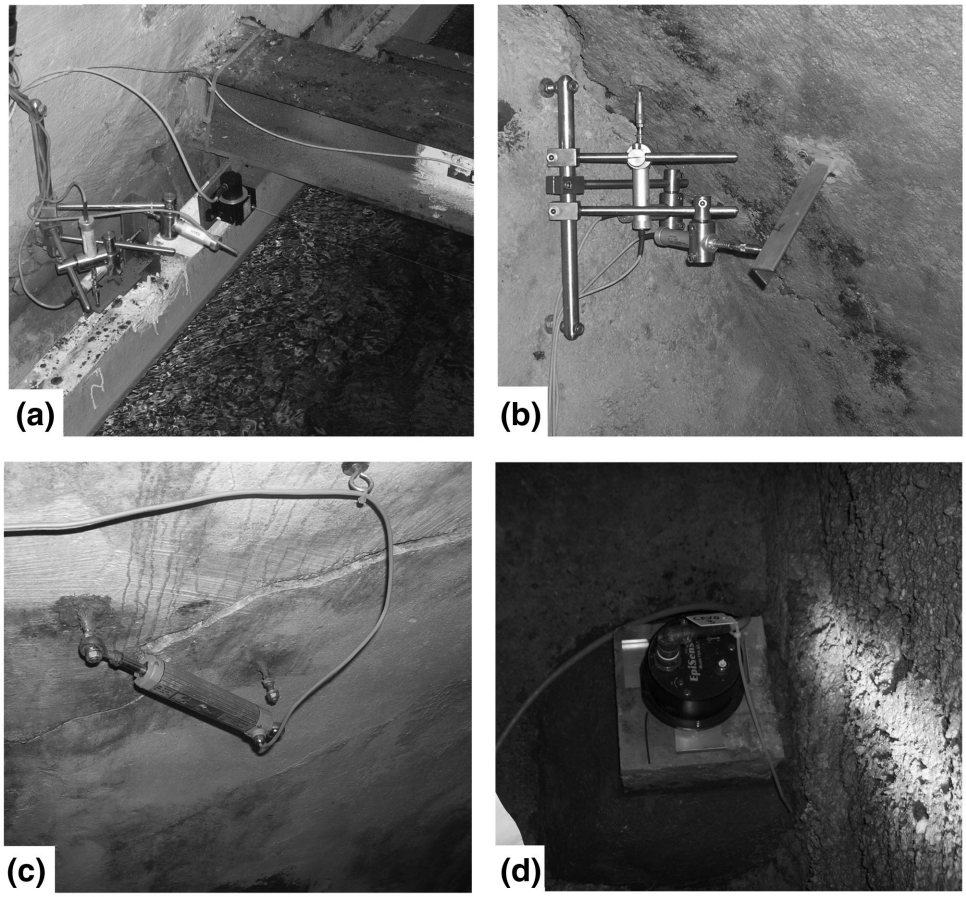

Figure 4. Examples of the monitoring system devices installed within the drainage tunnels of the Peschiera Spring aqueduct plant: (a) String and triaxial extensometer installation coupled with a strain gauge installed on structural reinforcements; (b) Triaxial extensometer, (c) Uniaxial extensometer; (d) Triaxial accelerometer installed on bedrock at the C1 station (see Fig. 1 for location).

physical properties of the recorded seismic signals in triggering displacements along the monitored joint.

2 EXPERIMENTAL DATA

Since September 2007, the stress–strain monitoring system has been recording the continuous gravitational deformations of the rock mass. This monitoring system (see Fig. 1 for location) consists of: eight strain gauges installed on structural reinforcements, seven string extensometers, 14 uniaxial extensometers and 15 triaxial extensometers (Figs 4a–c). All of the sensors have a displacement resolution of 0.1 μm and were set to automatically record at time intervals of 3 and 1 hr before and after October 2009, respectively. The records are collected by a local data logger and can be downloaded remotely.

On 2008 September 4, four accelerometric stations (GA, C1, F1 and C6; see Fig. 1 for location) were installed at approximately 414 m a.s.l. inside the slope in the drainage tunnels of the plant (Fig. 2). Each station was instrumented with a triaxial accelerometer (EPISENSOR from KINEMETRICS) directly installed on bedrock (Fig. 4d). The four accelerometers were connected via cable to a digital data logger (K2 from KINEMETRICS) with a 250 Hz sampling frequency, set to the absolute local time via a GPS device. According to the aim of the monitoring system, the data logger was set to record typologies of seismic events characterized by different duration and frequency content, that is ranging from micro-earthquakes (focused within the slope) to teleseismic events. To this end, some channels were set in Short-Term-Average/Long-Term-Average (STA/LTA) trigger mode, that improves the recording of weak motion; the others were set in amplitude threshold trigger mode, with specific thresholds derived from the analysis of the noise recorded by each channel. Moreover, bandpass filters in the range 0.1–15 and 2.5–50 Hz were alternatively applied in the trigger algorithm: the former is traditionally used in typical strong motion applications, while the latter is devoted to the detection of weak motion events. Two channels out of twelve are required to trigger the array, while the recorder detriggers when all the channels are below their specific detrigger level. The data logger was set with a 15 s pre- and post-event time; the latter is surely too short to enable the complete recording of coda waves, but resulted to be the best compromise as regards an efficient use of the recorder's data memory; practical values of post-event time are anyway too short in case of large distant earthquakes. Taking into account the applied setting of the data logger and the characteristics of the sensors, the data were processed in the frequency range 0.1–50 Hz.

Until June 2013, more than 1450 events were recorded by the accelerometric array. Since 2007, several deformational episodes have been observed by the stress–strain monitoring system. Among these episodes, it is possible to distinguish the following typologies: (i) deformational effects clearly related to earthquakes, which were classified as near-field events, RGE, and TSE; (ii) deformational

effects related to local micro-seismic events and corresponding to cracks or collapses occurring within the slope and (iii) deformational effects that cannot be related to the seismic records.

With respect to the first typology of episodes, it was observed that, in concomitance to one RGE and two TSE only, the monitoring system in joint J1 recorded mm-scale displacements (ranging from 0.7 up to 2 mm) cumulated in a few hours (Fig. 5). More in particular, the earthquake-induced displacements occurred within 20 hr after the 2008 December 23, Frignano (M_w 5.1) earthquake (Fig. 5b); within 6 hours after the 2009 January 15, Kuril Islands (M_w 7.3) earthquake (Fig. 5c) and within 1 hr after the 2011 March 11, Tohoku (M_w 9.0) earthquake (Fig. 5d). In all the cases, no significant variations of the karst aquifer discharge were recorded (Fig. 5). The deformational behaviour observed after the triggering earthquakes is significantly different from the one related to the MRC in which the whole slope is involved. As shown in Fig. 5a, this latter is characterized by an almost stationary strain rate of about 1 mm yr^{-1} resulting from long-time measures performed by the stress–strain sensors installed within the drainage plant. Moreover, as revealed by the azimuthal dip direction of the recorded displacements (Fig. 5a), the main direction of the whole landslide movement is almost NS oriented, although the average dip direction of the slope topography is about N45°W (Fig. 1).

Given these observations, this study was focused on the physical properties of the records having long and very long period waveforms only, to investigate on their triggering role. The records of earthquakes with moment magnitudes (M_w) $\geq$ 4.5 and epicentral distances >200 km (Fig. 6) were taken into account. As reported in Table 2, these events have epicentral distances in the range 200–9700 km and M_w values varying from 4.5 to 9.0. The recorded TSE include the 2008 M_w 7.9 Sichuan earthquake (China) and the 2011 M_w 9.0 Tohoku earthquake (Japan). The RGE include the 2012 Emilia M_w 5.9 earthquake (Italy) and the most recent 2013 Alpi Apuane M_w 5.2 earthquake (Italy).

A comparison between the recorded earthquakes and the worldwide seismicity that occurred during the monitored time interval (October 2008 to June 2013) is also reported in Fig. 6. This figure illustrates the location of all the earthquakes with $M_w > 7$ and (for the zoomed-in area) the earthquakes with $M_w > 5.5$ that have epicentral distances >500 km from the array. Based on these thresholds, the recorded events represent approximately 7 per cent of the earthquakes that occurred during the observation period. The earthquake locations are mainly concentrated along the southern boundaries of the Eurasian Plate, around the Pacific Plate and in the Mediterranean basin (including Spain, Italy, the Balkan Peninsula, Greece and Turkey). The recorded earthquakes are mainly located at the boundaries of the Eurasian plate.

The acceleration time histories of the 20 recorded events were analysed to understand the possible role of certain physical properties of the seismic signals with respect to their interaction with the jointed rock mass experiencing ongoing gravitational processes. Because the considered earthquakes have an epicentral distance at least 100 times larger than the accelerometric array dimensions, no significant differences among the recorded amplitudes at the four stations are observed for the same event. Therefore, this study uses only the records obtained at station C1, which has the highest signal-to-noise ratio. Site amplification effects at station C1 were excluded based on noise measurements that were processed by the GEOPSY software (Wathelet *et al.* 2011) according to the horizontal-to-vertical spectral ratio (HVSR) technique (Nakamura 1989; Fig. 7).

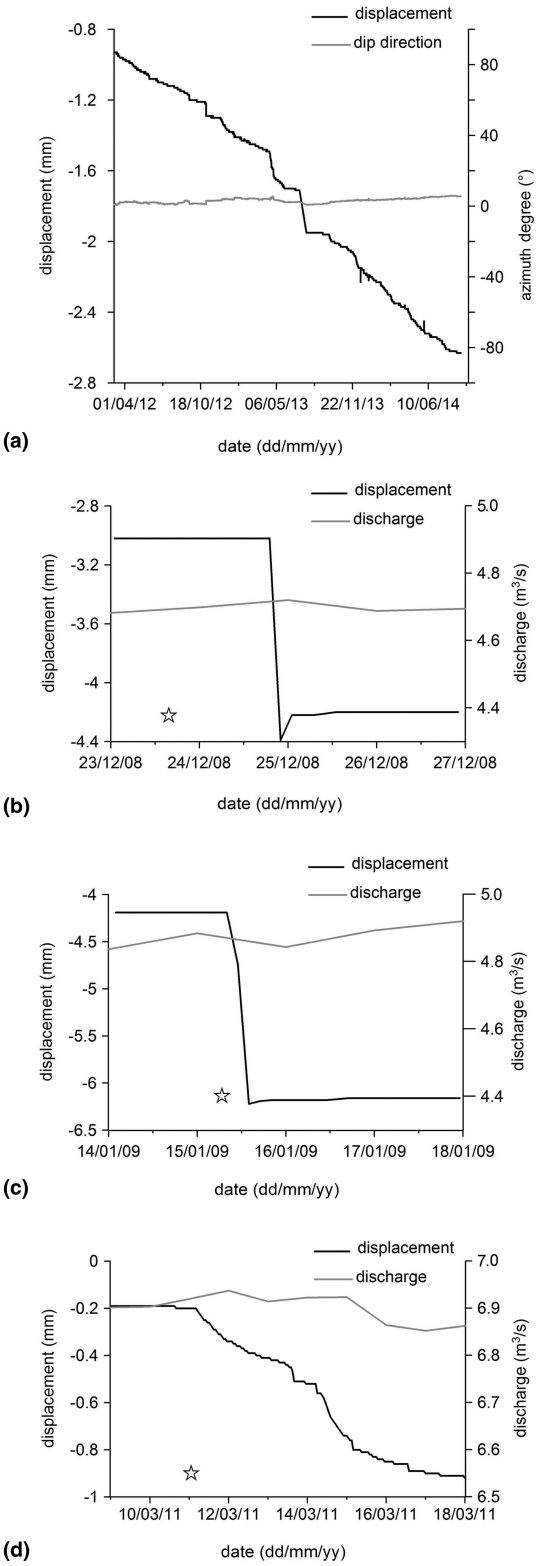

Figure 5. Total displacements recorded by the stress–strain monitoring system installed within the tunnels of the drainage plant and referred to: long-time displacement due to the MRC recorded during the 2012–2014 time interval (a); earthquake-induced displacements at the joint J1 due to the 2008 December 23, Frignano (M_w 5.1) earthquake (b), to the 2009 January 15, Kuril Islands (M_w 7.3) earthquake (c) and to the 2011 March 11, Tohoku (M_w 9.0) earthquake (d). The stars indicate the recording time of the earthquakes at the Peschiera Spring plant. The discharge of the karst aquifer is also reported.

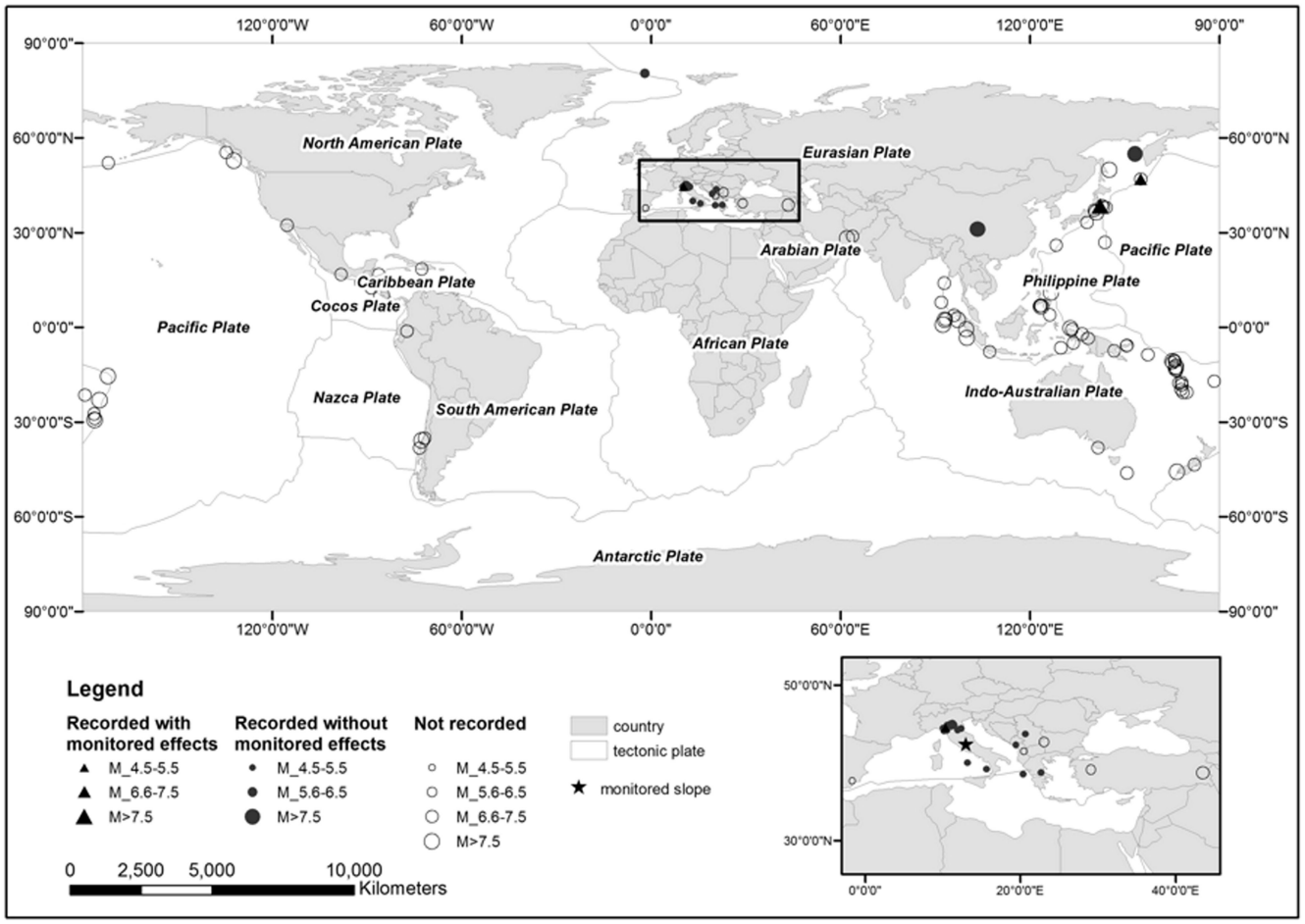

Figure 6. Spatial distribution and M_w class of the earthquakes that occurred worldwide between October 2008 and June 2013. For a better graphical resolution, the map only displays earthquakes with $M_w > 7$, whereas a zoomed window provides a detail of the Mediterranean basin ($M_w > 5.5$ and epicentral distances >500 km from the monitored slope). The 20 events recorded at the monitored slope and the three triggering events in particular are identified. The boundaries of the tectonic plates are also shown.

3 RESULTS

In this study we analyse the RGE and TSE recorded in the Peschiera Spring drainage plant between October 2008 and June 2013 as three of them were responsible for the previously described deformational episodes monitored at joint J1 (Figs 5b–d). Fig. 8 shows the acceleration time histories and the spectral amplitudes of the three triggering earthquakes as well as the trend of both the displacements recorded at joint J1 and the aquifer discharge in a monthly time window. The values of the aquifer discharge during the occurrence of the triggering earthquakes demonstrate that no changes in the water pressure occurred within the rock mass before the seismic events (Fig. 8c); Fig. 8(c) also shows that seasonally the discharge variations due to the aquifer are in the order of some cubic meters. Because the RGE and TSE that are responsible for the recorded joint displacements represent a limited sample (about 1 per cent) with respect to the potential trigger earthquakes (Fig. 6), a physical study of their seismic signals was performed via the Seismic Analysis Code (SAC) to search for specific physical properties that could have a role in the observed displacements. Due to the small number of recorded RGE and TSE, no statistical study could be performed; a trial and error procedure was followed to select the physical parameters that allow to distinguish the triggering events among the others.

First of all, the conventional kinematic and energy parameters (peak of ground acceleration – PGA, peak of ground velocity – PGV and Arias intensity – AI) were computed for the three main components (NS, UP and WE) of ground motion (Table 2). The arithmetic mean values of PGA, PGV and AI were also computed for the horizontal components of ground motion (hereafter referred to as $PGA_{\_H}$, $PGV_{\_H}$ and $AI_{\_H}$).

The AI was computed according to the following relationship (Arias 1970):

$$AI = \frac{\pi}{2g}\int_0^T a^2(t)\,\mathrm{d}t, \tag{1}$$

where g is the gravitational acceleration (9.81 m s^{-2}), a is the recorded acceleration (m s^{-2}), t is the time and T is the total duration of the seismic record.

As shown in Fig. 9(a), the $PGA_{\_H}$ values vary in the range of 10^{-5}–10^{-3} m s^{-2}, and the $AI_{\_H}$ values vary in the range of 10^{-10}–10^{-5} m s^{-1}. As it is expected, a good correlation exists between the $PGA_{\_H}$ and $AI_{\_H}$ values; however, the resulting distribution is not able to distinguish the three triggering seismic events from the others. The same result is obtained when considering the single horizontal components (i.e. parallel and normal to the direction of landslide movement) as well as the vertical component of ground motion.

In order to compare the landslide triggering with the strain effect associated with the RGE and TSE, the maximum strain change

Table 2. RGE and TSE recorded at station C1 by the accelerometric array installed in the Peschiera Spring slope and arranged by M_w and epicentral distance. The location, source area, M_w, epicentral distance, and depth were derived from the INGV website http://cnt.rm.ingv.it/ and the USGS website http://earthquake.usgs.gov/earthquakes/. PGA, PGV, AI (for each component of the ground motion: horizontal (_WE, _NS) and vertical (_UP), as well as for the arithmetic mean value of the horizontal components (_H)), PGA_{ratio} NS/WE, and AI_{ratio} NS/WE values, as well as the frequency value at the maximum of the FFT amplitude (f_max), were specifically computed for this study. The stars reported in the source area field refer to the three triggering events. Data that were not available are labelled na.

Date (dd/mm/yyyy)	Source area	M_w	Latitude	Longitude	Epicentral distance (km)	Depth (km)	PGA_WE ($m\,s^{-2}$)	PGA_NS ($m\,s^{-2}$)	PGA_UP ($m\,s^{-2}$)	PGA_H ($m\,s^{-2}$)	PGV_WE ($m\,s^{-1}$)	PGV_NS ($m\,s^{-1}$)	PGV_UP ($m\,s^{-1}$)	PGV_H ($m\,s^{-1}$)	AI_WE ($m\,s^{-1}$)	AI_NS ($m\,s^{-1}$)	AI_UP ($m\,s^{-1}$)	AI_H ($m\,s^{-1}$)	PGA_{ratio} NS/WE	AI_{ratio} NS/WE	f_{max} NS (Hz)	f_{max} WE (Hz)
3/11/2011	Tohoku* (Japan)	8.9	38.29°N	142.37°E	9700	24	1.65E-04	1.34E-04	1.76E-04	1.49E-04	1.63E-04	3.54E-04	4.35E-04	2.59E-04	3.70E-08	4.61E-08	7.83E-08	4.16E-08	0.81	1.25	0.06	0.06
5/24/2013	Okhots Sea (Russia)	8.2	54.91°N	153.34°E	9500	609	1.95E-03	1.95E-03	2.06E-03	1.95E-03	4.12E-04	3.39E-04	4.74E-04	3.76E-04	3.66E-06	3.14E-06	3.32E-06	3.40E-06	1.00	0.86	1.3	1.0
5/12/2008	Sichuan (China)	7.9	30.98°N	103.36°E	7800	35	2.15E-04	1.01E-04	1.46E-04	1.58E-04	1.04E-02	9.55E-03	6.02E-03	9.97E-03	5.09E-08	2.82E-08	4.01E-08	3.95E-08	0.47	1.47	1.0	1.0
1/15/2009	Kuril Islands* (Russia)	7.3	46.86°N	155.15°E	9300	35	7.24E-05	1.14E-04	1.21E-04	9.31E-05	6.05E-04	8.80E-04	8.19E-04	7.43E-04	6.45E-09	1.37E-08	1.10E-08	1.01E-08	1.57	1.31	0.8	0.8
3/6/2009	Greenland	6.5	80.37°N	01.87°W	4000	10	2.45E-05	2.65E-05	1.70E-05	2.55E-05	1.91E-04	1.71E-04	1.51E-04	1.81E-04	7.47E-10	1.16E-09	3.77E-10	9.55E-10	1.08	0.96	0.6	0.6
5/20/2012	Emilia (Italy)	5.9	44.89°N	11.23°E	315	6	5.85E-03	8.58E-03	5.82E-03	7.21E-03	1.83E-03	2.12E-03	1.58E-03	1.97E-03	4.51E-05	5.07E-05	2.75E-05	4.79E-05	1.47	1.13	0.6	0.8
5/29/2012	Emilia (Italy)	5.8	44.85°N	11.08°E	315	10	3.62E-03	3.37E-03	2.28E-03	3.50E-03	8.75E-04	9.43E-04	8.26E-04	9.09E-04	1.05E-05	1.17E-05	6.21E-06	1.11E-05	0.93	1.11	1.0	0.4
11/3/2010	Serbia	5.4	43.72°N	20.62°E	640	10	7.12E-04	6.61E-04	4.53E-04	6.86E-04	1.33E-04	1.17E-04	8.44E-05	1.25E-04	2.75E-07	3.14E-07	1.36E-07	2.95E-07	0.93	1.14	0.7	0.7
1/27/2012	Frignano (Italy)	5.4	44.48°N	10.03°E	340	61	7.23E-04	6.88E-04	8.76E-04	7.06E-04	1.13E-04	8.64E-05	8.87E-05	9.99E-05	4.79E-07	4.60E-07	4.60E-07	4.70E-07	0.95	0.96	2.0	1.5
12/17/2008	South Tyrrhenian Sea (Italy)	5.3	39.16°N	15.58°E	403	218	9.90E-05	7.78E-05	7.57E-05	8.84E-05	1.03E-03	6.67E-04	7.42E-04	8.48E-04	5.65E-09	7.88E-09	4.72E-09	6.77E-09	0.79	0.97	0.7	1.5
11/3/2010	South Tyrrhenian Sea (Italy)	5.3	39.99°N	13.16°E	265	486	2.88E-04	2.04E-04	6.49E-04	2.46E-04	8.56E-05	4.10E-05	1.05E-04	6.33E-05	5.62E-08	4.05E-08	7.41E-08	4.84E-08	0.71	0.72	0.8	0.5
6/21/2013	Alpi Apuane (Italy)	5.2	44.15°N	10.14°E	300	5	1.24E-03	1.20E-03	1.27E-03	1.22E-03	2.77E-04	2.14E-04	1.99E-04	2.46E-04	1.20E-06	1.37E-06	8.71E-07	1.29E-06	0.97	1.14	0.5	1.0
12/13/2008	Greece	5.1	38.73°N	22.62°E	910	12	3.41E-05	4.26E-05	2.71E-05	3.83E-05	3.20E-04	3.28E-04	2.94E-04	3.24E-04	2.12E-09	2.89E-09	1.08E-09	2.51E-09	1.25	0.95	1.0	1.1
12/23/2008	Frignano* (Italy)	5.1	44.52°N	10.35°E	330	27	1.07E-03	1.78E-03	1.22E-03	1.42E-03	1.68E-04	2.92E-04	1.38E-04	2.30E-04	9.81E-07	1.26E-06	6.42E-07	1.12E-06	1.67	1.28	0.8	1.2
1/8/2009	Albania	4.9	na	na	652	2	9.53E-05	1.03E-04	9.90E-05	1.07E-03	9.15E-04	9.01E-04	9.93E-04	7.46E-09	9.44E-09	7.00E-09	8.45E-09	1.08	0.86	0.8	1.1
1/25/2012	Parma (Italy)	4.9	44.85°N	10.53°E	340	33	4.92E-04	5.04E-04	3.33E-04	4.98E-04	1.07E-04	1.23E-04	7.19E-05	1.15E-04	1.74E-07	1.78E-07	1.11E-07	1.76E-07	1.02	1.02	1.0	1.5
2/1/2009	Greece	4.8	38.55°N	20.32°E	750	20	1.38E-05	1.82E-05	1.90E-05	1.60E-05	1.40E-04	1.60E-04	1.64E-04	1.50E-04	5.37E-11	1.16E-10	9.58E-11	8.50E-11	1.32	1.58	1.2	1.5
4/5/2009	Forlì (Italy)	4.6	44.23°N	11.91°E	230	28	8.67E-04	1.00E-03	7.62E-04	9.36E-04	1.29E-04	1.89E-04	1.08E-04	1.59E-04	6.88E-07	7.11E-07	5.02E-07	6.99E-07	1.16	1.03	1.0	1.0
2/11/2010	Albania	4.5	42.28°N	19.43°E	580	20	2.50E-04	2.90E-04	2.19E-04	2.70E-04	4.52E-05	3.80E-05	5.63E-05	4.16E-05	2.58E-08	2.65E-08	2.52E-08	2.62E-08	1.16	1.03	1.5	0.2
6/6/2012	Ravenna (Italy)	4.5	42.28°N	19.43°E	235	26	4.04E-04	5.16E-04	3.34E-04	4.60E-04	9.73E-05	7.03E-05	5.47E-05	8.38E-05	1.53E-07	1.78E-07	1.01E-07	1.65E-07	1.28	1.17	2.0	1.5

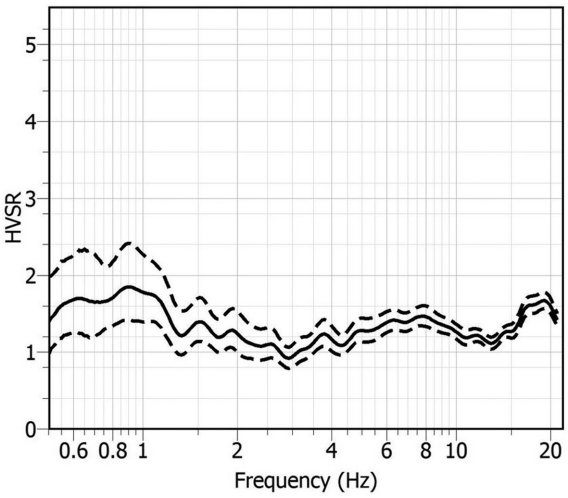

Figure 7. HVSR by noise measurements at station C1 showing no significant resonance effects (i.e. no peaks with amplitudes >2).

due to the passage of seismic surface waves was estimated. As the landslide movement recorded so far is NS oriented (Fig. 5a), the horizontal components of the surface ground motion, mainly related to Love waves (Lw), were analized. Taking into account that the records were obtained in the tunnels of the drainage plant, that is at the interface between saturated and unsaturated limestones located about 100 m below the ground surface, a single-layered half-space model was assumed to perform a dispersion analysis of Lw according to the equation (Aki & Richards 1980):

$$\tan\left[2\pi f \cdot h\left(1/V_1^2 - 1/V_L^2(f)\right)^{0.5}\right] = G_2/G_1\left[\left(1/V_R^2(f) - 1/V_2^2\right)^{0.5} / \left(1/V_1^2 - 1/V_L^2(f)\right)^{0.5}\right], \quad (2)$$

where f is the frequency of the representative sinusoidal waveform, h is the thickness of the layer that overlies the elastic half-space, G_1 and G_2 are the shear modulus of the layer and the elastic half-space respectively, V_1 and V_2 are the shear wave velocity of the layer and the elastic half-space, respectively, $V_L(f)$ is the velocity of the Lw propagating horizontally at the free-field interface.

More in particular, the following parameters were attributed:

$$h = 100\,\text{m},\ G_1 = 17.7\,\text{GPa},\ G_2 = 18.0\,\text{GPa},\ V_1 = 1693\,\text{m s}^{-1},\ V_2 = 1708\,\text{m s}^{-1}.$$

To solve eq. (2) the predominant frequency (f_{Dmax}) of each displacement waveform was obtained from the recorded time histories by integration after filtering in the range 0.001–50 Hz. It was assumed that the direction of Lw propagation were NS and WE alternatively, due to the lack of strong polarization evidences. The f_{Dmax} values range from 0.015 up to 0.3 Hz and the resulting V_L are very close to the V_2 value (i.e. the maximum admissible value). The k ($= 2\pi f_{Dmax}/V_L$) values were computed to derive the strain change along both NS (ε_{NS}) and WE (ε_{WE}) direction in the form (Aki & Richards 1980):

$$\varepsilon = D(t) \cdot k/2, \quad (3)$$

where $D(t)$ is the displacement time history pass-band filtered in a narrow frequency range (±10 per cent of f_{Dmax}), to be consistent with the waveform assumed by eq. (2).

The obtained results (Fig. 9b) show that the Tohoku earthquake only can be distinguished among the others as it is characterized

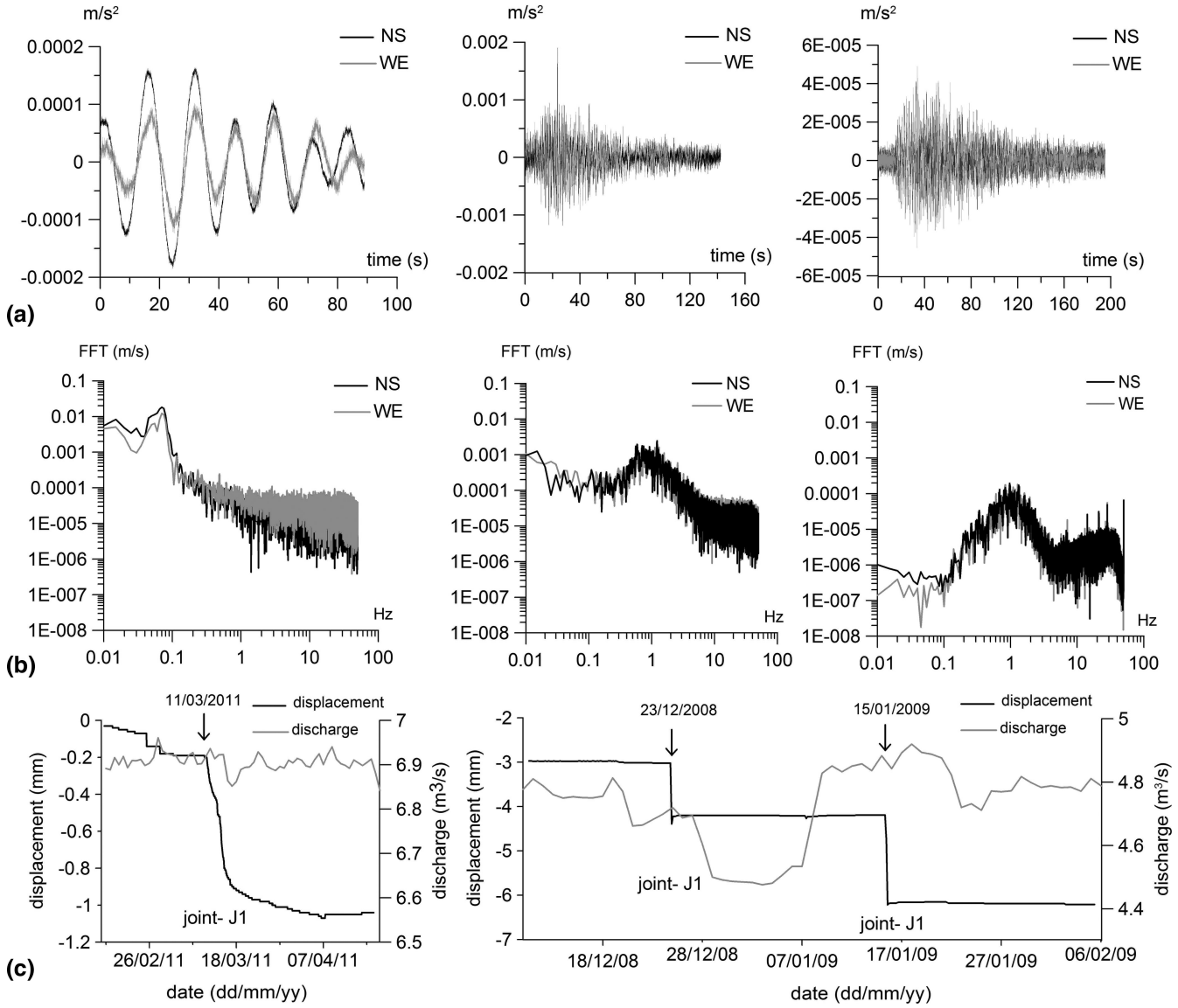

Figure 8. 2011 March 11, Tohoku (M_w 9.0) teleseismic event (left-hand panel), 2008 December 23, Frignano (M_w 5.1) earthquake (centre panel) and the 2009 January 15, Kuril Islands (M_w 7.3) earthquake (right-hand panel) recorded at station C1 (location in Fig. 1): (a) Horizontal acceleration time histories; (b) FFT of the two horizontal components of the ground motion (left: NS; right: WE); and (c) Earthquake-triggered displacements monitored at joint J1 of Fig. 1. The aquifer discharge in the same time interval is also reported.

by the maximum ε_{NS} and ε_{WE} values. It is remarkable that the waveform of the most distant recorded TSE was capable to generate the maximum strain changes although it was characterized by $PGA_{\_H}$ and $AI_{\_H}$ values close to the average of all the recorded RGE and TSE.

To investigate the role of seismic ground motion in relation to the landslide movement direction, the ratios between the NS and WE components were computed for both the PGA and AI parameters ($PGA_{\_ratio}$ and $AI_{\_ratio}$, respectively). The $PGA_{\_ratio}$ values vary in the range of 0.4–1.6, and the $AI_{\_ratio}$ values vary in the range of 0.6–1.6 (Fig. 9c). The resulting distribution indicates that the three triggering earthquakes are characterized by an $AI_{\_ratio}$ higher than 1.2, whereas the related $PGA_{\_ratio}$ values lay in the upper portion of the distribution. Given that two more records (corresponding to the 2008 May 12, M_w 7.9 Sichuan earthquake and the 2009 February 1, M_w 4.8 Greece earthquake) exceed the 1.2 threshold (Fig. 9c), the above considered parameters are only partially able to distinguish the triggering events from the others. On the contrary, the distribution of the ratios between NS and UP components, computed for PGA and AI, does not allow to distinguish the three triggering events among the others.

Based on these results, an analysis in the frequency domain was performed by computing the fast Fourier transform (FFT) of the recorded horizontal accelerometric signals.

Because the NS/WE $AI_{\_ratio}$ which partially distinguishes the triggering earthquakes from the others is higher than 1, the frequency content of the NS components (i.e. parallel to the horizontal component of the landslide movement as shown in Fig. 1) of the recorded signals was analysed in more detail.

This analysis indicated that in contrast to the 2008 Sichuan and 2009 Greece earthquakes, the three triggering earthquakes are characterized by peak frequencies lower than 1 Hz for the FFT amplitude of the NS component (i.e. in the range of 0.06–0.8 Hz). To illustrate this result, Fig. 8a, presents the time history and FFT (Fig. 8b) of

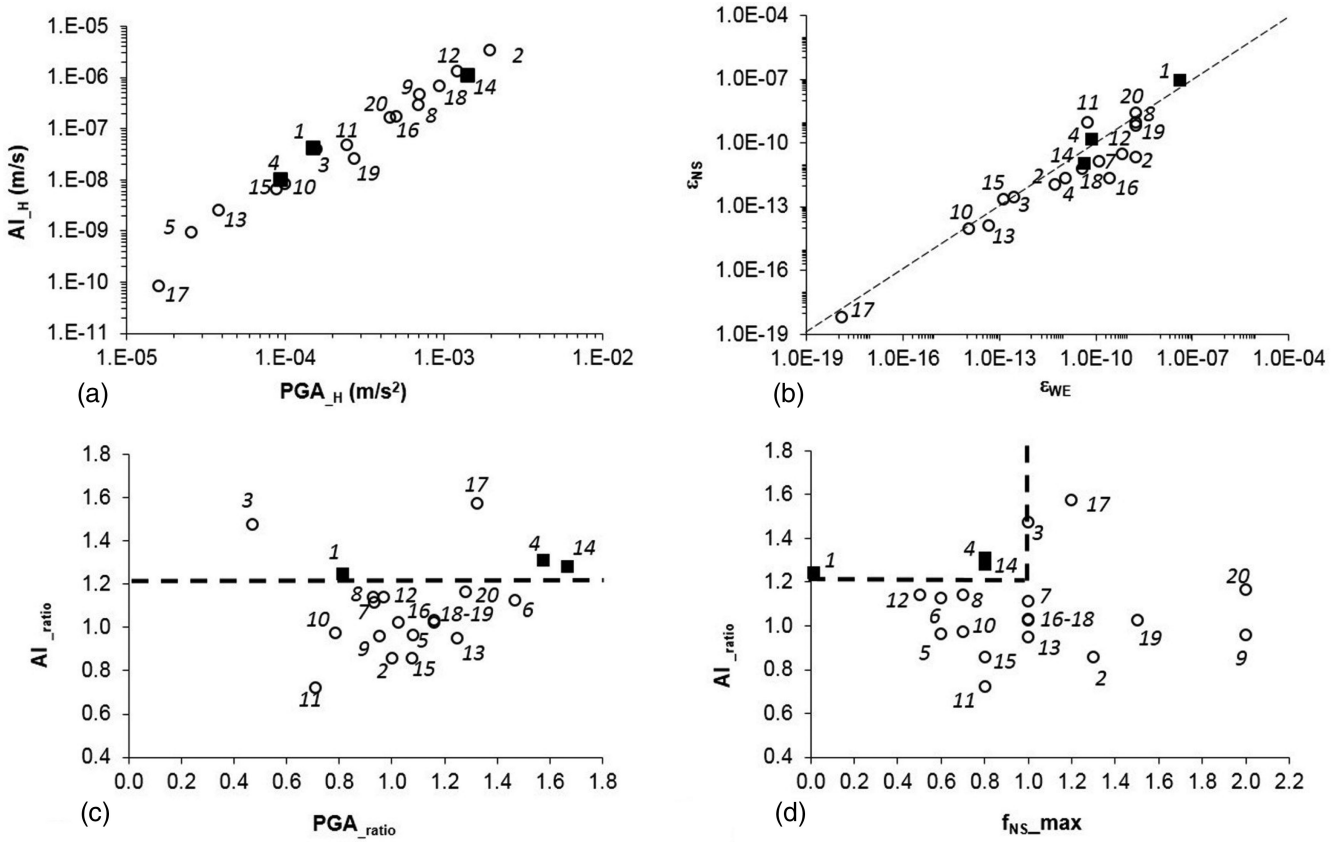

Figure 9. Distribution of the physical parameters of the RGE and TSE recorded at station C1 of Fig. 1 considered to distinguish the triggering events: (a) the $AI_{\_H}$ versus $PGA_{\_H}$ absolute value distribution is unable to distinguish the three events; (b) the ε_{NS} versus ε_{WE} distribution allow to distinguish the Tohoku earthquake only; (c) the $AI_{\_ratio}$ versus $PGA_{\_ratio}$ relative value distribution indicates the reliability of the $AI_{\_ratio}$ for establishing the minimum threshold of 1.2 to partially distinguish the three events; (d) the $AI_{\_ratio}$ versus $f_{\_max}$ NS distribution is suitable for establishing the minimum threshold of the $AI_{\_ratio}$ (1.2) and the maximum threshold of $f_{\_max}$ NS (1 Hz) that completely allow to distinguish the triggering events from the others.

the two horizontal components recorded at station C1 (Fig. 1) for the 2011, Tohoku TSE (M_w 9.0, in Table 2), the 2008, Frignano (M_w 5.1) RGE, and the 2009, Kuril Islands (M_w 7.3) RGE. The FFT values exhibit maximum amplitudes at a frequencies lower than 0.2 Hz. Moreover, the FFT amplitude of the NS component is approximately two-fold higher than the WE component. Therefore, the distribution of the $AI_{\_ratio}$ versus the frequency of the FFT peak of the NS component ($f_{\_max}$ NS) allows the triggering earthquakes to be distinguished within the complete dataset of the accelerometric records (Fig. 9d). In particular, the parametric conditions that seem able to trigger joint displacements correspond to $AI_{\_ratio}$ values higher than 1.2 and frequencies of the FFT peaks of the horizontal component of ground motion parallel to the horizontal landslide movement lower than 1 Hz.

4 DISCUSSION

The here reported findings indicate that the triggering of the observed displacements induced by RGE and TSE is controlled by the following properties: (i) the distribution of relative energy and PGA of the horizontal components of the signal and (ii) the spectral amplitude distribution in the frequency domain.

These properties are in agreement with the gravity-induced slope deformation mechanism (i.e., movement direction and boundary geometry) and with the dimensions of the whole involved rock mass volume. As already discussed by some authors (Rubinstein *et al.* 2007; Miyazawa & Brodsky 2008; Jousset & Rohmer 2012) the surface Rayleigh and Love waves can be regarded as responsible for triggering movements along discontinuities and related effects (among which volcanic activity and microtremors) due to relevant changes in the local stress field. Nevertheless, the here obtained results demonstrate that the displacements triggered by RGE and TSE along joint J1 have to be related to a rock-mass/earthquake interaction rather than to a single-joint/earthquake interaction. In this regard, the displacements triggered along a single joint reveal that, in effect, they are induced within the entire landslide mass.

As a matter of fact: (i) the higher ground motion energy and PGA of the NS component respect to the WE one are coherent with the recorded landslide movement that mainly occurs in the NS direction and (ii) the higher efficiency of long to very long periods to produce a seismic response of the landslide mass is linked to its km-scale dimensions.

The significance of the measured displacements triggered by the three RGE and TSE is proved by their amplitudes (up to 2 mm), which are on the same order of magnitude as the average annual cumulative displacement observed over a decade of strain measurements made within the slope (Martino *et al.* 2004; Lenti *et al.* 2012). Moreover, as illustrated by the aquifer discharge trend in Figs 5(b)–(d) and 7(c), no significant variations in the water pressure occurred when the earthquake-induced displacements at joint J1 were recorded.

This study demonstrates that only RGE and TSE characterized by peculiar values for certain physical parameters related to both

energy and spectral contributions are capable of triggering displacements along joints in the monitored slope.

If the recurrence of triggering earthquakes were comparable with the average occurrence of RGE and TSE (which is in the order of several tens per year), the induced strain effects (in the order of one decimeter per year), would not be compatible with the landform evolution actually observed on the Peschiera Spring slope as well as with the strain effects observed within the tunnels of the drainage plant. Indeed, as these last ones were realized during the 1930s of the last century, meter-scale displacements should have been observed as an effect of impulsive displacements only, that is due to occurred RGE and TSE. Moreover, as the geological evolution of the actual slope can be referred to several thousands of years (Martino *et al.* 2004 and references therein), the displacements due to impulsive strain effects should have induced unstable slope conditions. On the contrary, based on the previous considerations, the geological evolution of the landforms in the Peschiera Spring slope demonstrates that the MRC is dominant with respect to impulsive deformational episodes.

This study demonstrates that the MRC affecting the Peschiera Spring slope can be accelerated by transient dynamic events, such as earthquakes having suitable physical properties. Thus, the increased strain rate of the MRC represents an out-of-trend effect that can reduce the delay time of a generalized failure. In this regard, a possible future evolution of the Peschiera Spring slope is exemplified by the La Clapière DSGD case history in France (Booth *et al.* 2013; see also the web site: http://gravitaire.oca.eu), where a displacement rate in the order of metres per year was measured since 1987 and lead to a generalized failure of the slope, associated to a very evident evolution of the landforms, such as increasing height of the pre-existing scarps and generation of new ones.

5 CONCLUSIONS

This study demonstrates that RGE and TSE can be responsible for triggering deformations along rock mass joints, as measured in Central Italy by an integrated displacement and accelerometric monitoring system. The observed displacements can be attributed to the seismic input because no other relevant variation in the slope conditions (such as water pressure changes or human-induced actions) occurred. On the other hand, the stationary rate of the landslide induced strains is too low for justifying the millimetre-scale displacements occurred within a few hours. An analysis of the recorded triggering earthquakes compared to several other records of RGE and TSE allowed for pointing out some physical properties of the triggering earthquakes that could explain the induced displacements. The results of this analysis demonstrate that long to very long seismic periods and ground motion amplitudes larger in the NS direction (i.e. corresponding to the main direction of the landslide movement) represent the key combination of properties that distinguish the triggering earthquakes from the others. The here presented study has not a statistical meaning due to the reduced number of samples, that is conditioned by the rarity of the considered events; nevertheless, it provides a contribution to better understand the conditions for which landslides can be sensitive to remote earthquakes.

The rarity of occurrence of RGE- and TSE-triggered displacements is compatible with the existing landforms and the actual equilibrium conditions of the slope. If all of the worldwide occurred earthquakes could cause strain effects comparable to those induced by the triggering ones, meter-scale displacements would have been observed within some tens of years and generalized failures and collapses should be visible on the slope.

ACKNOWLEDGEMENTS

The authors wish to thank C. Romagnoli and G. Martino of the ACEA S.p.A. for providing the data of the Peschiera Spring accelerometric array. The authors also thank Bill Murphy for the precious suggestions given to improve this study, Philippe Jousset and another anonymous reviewer for the useful revisions to this paper.

REFERENCES

Aki, K. & Richards, P.G., 1980. *Quantitative Seismology, Theory and Methods,* 2 Vols, W.H. Freeman and Co., 948 pp.

Alfaro, P., Delgado, J., Garcia-Tortosa, F.J., Lenti, L., Lopez, J.A., Lopez-Casado, C. & Martino, S., 2012. Widespread landslides induced by the M_w 5.1 earthquake of 11 May 2011 in Lorca, SE Spain, *Eng. Geol.,* **137–138,** 40–52.

Arias, A., 1970. A measure of earthquake intensity, in *Seismic Design for Nuclear Power Plants,* pp. 438–483, ed. Hansen, R.J., MIT Press.

Booth, A.M., Lamb, M.P., Avouac, J.P. & Delacourt, C., 2013. Landslide velocity, thickness, and rheology from remote sensing: La Clapière landslide, France, *Geophys. Res. Lett.,* **40,** 4299–4304.

Bozzano, F., Lenti, L., Martino, S., Paciello, A. & Scarascia Mugnozza, G., 2011. Evidences of landslide earthquake triggering due to self-excitation process, *Int. J. Earth Sci.,* **100,** 861–879.

Brodsky, E.E., Gordeev, E. & Kanamori, H., 2003. Landslide basal friction as measured by seismic waves, *Geophys. Res. Lett.,* **30**(24), 2236, doi:10.1029/2003GL018485.

Chigira, M., 1992. Long-term gravitational deformation of rocks by mass rock creep, *Eng. Geol.,* **32,** 157–184.

Delgado, J., Garrido, J., Lopez-Casado, C., Martino, S. & Pelaez, J.A., 2011. On far field occurrence of seismically induced landslides, *Eng. Geol.,* **123,** 204–213.

Hollingsworth, J., Jackson, J., Alarcón, J.E., Bommer, J.J. & Bolourchi, M.J., 2007. The 4th February 1997 Bojnurd (Garmkhan) earthquake in NE Iran: field, teleseismic, and strong-motion evidence for rupture directivity effects on a strike-slip fault, *J. Earthq. Eng.,* **11,** 193–214.

Hutchinson, J.N., 1988. General report: morphological and geotechnical parameters of landslides in relation to geology and hydrogeology, in *Proceedings of the 5th International Symposium on Landslides,* Lausanne, Balkema, Rotterdam, pp. 3–36.

Itaba, S. & Ando, R., 2011. A slow slip event triggered by teleseismic surface waves, *Geophys. Res. Lett.,* **38,** L21306, doi:10.1029/2011GL049593.

Johnston, M.J.S. & Mauk, F.J., 1972. Earth tides and the triggering of eruptions from Mt. Stromboli, Italy, *Nature,* **239,** 266–267.

Jousset, P. & Rohmer, J., 2012. Evidence for remotely triggered microearthquakes during salt cavern collapse, *Geophys. J. Int.,* **191,** 207–223

Jousset, P. *et al.*, 2013. Signs of magma ascent in LP and VLP seismic events and link to degassing: an example from the 2010 explosive eruption at Merapi volcano, Indonesia, *J. Volc. Geotherm. Res.,* **261,** 171–192.

Kasahara, J., 2002. Tides, earthquakes and volcanoes, *Science,* **297,** 348–349.

Lenti, L., Martino, S., Paciello, A., Prestininzi, A. & Rivellino, S., 2012. Microseismicity within a karstified rock mass due to cracks and collapses triggered by earthquakes and gravitational deformations, *Nat. Hazards,* **64,** 359–379.

Maffei, A., Martino, S. & Prestininzi, A., 2005. From the geological to the numerical model in the analysis of the gravity-induced slope deformations: an example from the Central Apennines (Italy), *Eng. Geol.,* **78,** 215–236.

Martino, S., Prestininzi, A. & Scarascia Mugnozza, G., 2004. Geological-evolutionary model of a gravity-induced slope deformation in the carbonate central Apennines (Italy), *Q. J. Eng. Geol. Hydr.,* **37**(1), 31–47.

McNutt, S.R. & Beavan, R.J., 1981. Volcanic earthquakes at Pavlof volcano correlated with the solid Earth tide, *Nature,* **294,** 615–618.

Miyazawa, M. & Brodsky, E.E., 2008. Deep low-frequency tremor that correlates with passing surface waves, *J. geophys. Res.,* **113,** B01307, doi:10.1029/2006JB004890.

Myiazawa, M., Nakanishi, I., Sudo, Y. & Ohkura, T., 2005. Dynamic response of frequent tremors at Aso volcano to teleseismic waves from the 1999 Chi-Chi, Taiwan earthquake, *J. Volc. Geotherm. Res.,* **147,** 173–186.

Nakamura, Y., 1989. A method for dynamic characteristics estimation of subsurface using microtremor on the ground surface, *Q. Rep. RTRI,* **30**(1), 25–33.

Pomeroy, P.W., Best, W.J. & McEvilly, T.V., 1982. Test ban treaty verification with regional data—a review, *Bull. seism. Soc. Am.,* **72,** S89–S129.

Rodríguez, C.E., Bommer, J.J. & Chandler, R.J., 1999. Earthquake-induced landslides: 1980–1997, *Soil Dyn. Earthq. Eng.,* **18,** 325–346.

Rubinstein, J.L., Vidale, J.E., Gomberg, J., Bodin, P., Creager, K.C. & Malone, S.D., 2007. Non-volcanic tremor driven by large transient shear stresses, *Nature,* **448,** 579–582.

Rydelek, P.A., Davis, D.M. & Koyanagi, P.Y., 1988. Tidal triggering of earthquakes swarms at Kilauea Volcano, Hawaii, *J. geophys. Res.,* **93**(B5), 4401–4411.

Savage, W.Z. & Varnes, D.J., 1987. Mechanism of gravitational spreading of steep-sided ridges ("sackung"), *Bull. Int. As Eng. Geol.,* **35,** 31–36.

Sepulveda, S.A., Murphy, W. & Petley, D.N., 2005a. Topographic controls on coseismic rock slides during the 1999 Chi-Chi earthquake, Taiwan, *Q. J. Eng. Geol. Hydrogeol.,* **38,** 189–196.

Sepulveda, S.A., Murphy, W., Jibson, R.W. & Petley, D.N., 2005b. Seismically induced rock slope failures resulting from topographic amplification of strong ground motions: the case of Pacoima Canyon, California, *Eng. Geol.,* **80,** 336–348.

Sottili, G., Martino, S., Palladino, D.M., Paciello, A. & Bozzano, F., 2007. Effects of tidal stresses on volcanic activity at Mount Etna, Italy, *Geophys. Res. Lett.,* **34,** L01311, doi:10.1029/2006GL028190.

Van der Elst, N.J. & Brodsky, E.E., 2010. Connecting near field and far field earthquake triggering to dynamic strain, *J. geophys. Res.,* **115,** B07311, doi:10.1029/2009JB006681.

Wathelet, M., Orhnberger, M., Köhler, A. & Cornou, C., 2011. Geophysical signal database for noise array processing (GEOPSY – release 2.7.4), Available at: http://www.geopsy.org/download.php, last accessed December 2014.

Zischinsky, U., 1969. Uber Sackungen, *Rock Mech.,* **1,** 30–52.